JGR Space Physics

RESEARCH ARTICLE
10.1029/2024JA032447

Key Points:

- The TEC response showed latitudinal variances, with a 25%–40% decrease in midlatitudes but only a 10%–25% reduction in the equatorial region
- The Ne response showed altitudinal dependencies, with a larger depletion and a slower recovery near the F2 peak height than below and above
- The NmF2 exhibited a 30%–50% reduction, and the hmF2 exhibited a 20–30 km decrease in the recovery phase after the maximum obscuration

Supporting Information:

Supporting Information may be found in the online version of this article.

Correspondence to:

E. Aa,
aercha@mit.edu

Citation:

Aa, E., Coster, A. J., Zhang, S.-R., Vierinen, J., Erickson, P. J., Goncharenko, L. P., & Rideout, W. (2024). 2-D total electron content and 3-D ionospheric electron density variations during the 14 October 2023 annular solar eclipse. *Journal of Geophysical Research: Space Physics*, *129*, e2024JA032447. https://doi.org/10.1029/2024JA032447

Received 11 JAN 2024
Accepted 29 FEB 2024

2-D Total Electron Content and 3-D Ionospheric Electron Density Variations During the 14 October 2023 Annular Solar Eclipse

Ercha Aa[1], Anthea J. Coster[1], Shun-Rong Zhang[1], Juha Vierinen[2], Philip J. Erickson[1], Larisa P. Goncharenko[1], and William Rideout[1]

[1]Haystack Observatory, Massachusetts Institute of Technology, Westford, MA, USA, [2]Department of Physics and Technology, The Arctic University of Norway, Tromsø, Norway

Abstract This study investigates the ionospheric total electron content (TEC) responses in the 2-D spatial domain and electron density variations in the 3-D spatial domain during the annular solar eclipse on 14 October 2023, using ground-based Global Navigation Satellite System (GNSS) observations, a novel TEC-based ionospheric data assimilation system (TIDAS), ionosonde measurements, and satellite in situ data. The main results are summarized as follows: (a) The 2-D TEC responses exhibited distinct latitudinal differences. The mid-latitude ionosphere exhibited a more substantial TEC decrease of 25%–40% along with an extended recovery time of 3–4 hr. In contrast, the equatorial and low-latitude ionosphere experienced a smaller TEC reduction of 10%–25% and a faster recovery time of 20–50 min. The minimal eclipse effect was observed near the northern equatorial ionization anomaly crest region. (b) The ionospheric electron density variations during the eclipse were effectively reconstructed by TIDAS data assimilation in the 3-D domain, providing important altitude information with validity. (c) The ionospheric electron density variations showed a notable altitude-dependent feature. The eclipse led to a substantial electron density reduction of 30%–50%, with the maximum depletion occurring around the ionospheric F2-layer peak height (hmF2) of 250–350 km. The post-eclipse recovery of electron density exhibited a relatively slower pace near the F2-layer peak height than that at lower and higher altitudes.

Plain Language Summary On 14 October 2023, the Great American annular solar eclipse traversed North, Central, and South America with dense observational network in place, presenting a valuable opportunity for exploring the eclipse-induced ionospheric responses from mid-latitude to equatorial regions. This paper presents a comprehensive analysis of the 2-D ionospheric TEC and 3-D electron density responses during the eclipse, utilizing dense ground-based GNSS observations, a new TEC-based ionospheric data assimilation system (TIDAS), and ionosonde and satellite data sets. The TIDAS data assimilation system provides accurate and reliable regional ionospheric electron density reconstruction, which can effectively reproduce the electron density variations during the eclipse in the 3-D domain with important altitude information and high-fidelity details. This multi-instrumental and data assimilation study highlights the latitudinal and altitudinal dependencies of the eclipse-induced ionospheric responses, advancing the current understanding of how a solar eclipse event impacts the ionosphere.

1. Introduction

A solar eclipse is a stunning celestial occurrence and serves as a naturally active experiment that offers exceptional opportunities to explore the effects of transient changes in solar radiation on the ionosphere. Over the past several decades, researchers have extensively explored the impacts of solar eclipses on the ionosphere utilizing a variety of ground-based and space-based measurements, such as plasma temperature, velocity, and density measurements from powerful incoherent scatter radars (e.g., Goncharenko et al., 2018; MacPherson et al., 2000; Momani et al., 2010; Salah et al., 1986), ionospheric peak height and electron density observations from individual ionosondes (e.g., G. Chen et al., 2013; Dear et al., 2020; Evans, 1965; Farges et al., 2001; Reinisch et al., 2018), Global Navigation Satellite Systems (GNSS) total electron content (TEC) data (e.g., Aa et al., 2021; Cherniak & Zakharenkova, 2018; Coster et al., 2017; Ding et al., 2010; Huang et al., 2020; Jakowski et al., 2008; Silwal et al., 2021; Sun et al., 2018; Zhang et al., 2017, 2021), as well as satellite measurements (e.g., Aa et al., 2020; Aryal et al., 2020; Hairston et al., 2018; Perry et al., 2019). Furthermore, the ionosphere-thermosphere response to solar eclipse has been widely investigated using numerical simulations and/or data assimilation techniques (e.g., Aa, Zhang, et al., 2023; C.-H. Chen et al., 2019; Cnossen et al., 2019; Dang et al., 2018; Huba & Drob, 2017; Le et al., 2020; Lei et al., 2018; Lin et al., 2023; Müller-Wodarg et al., 1998; Wang et al., 2019; Wu et al., 2018).

The eclipse-induced direct ionospheric effect includes a depletion of a few tenths in ionospheric electron density and TEC due to a local decrease of the photo-ionization (e.g., Afraimovich et al., 1998; Rishbeth, 1968; Tsai & Liu, 1999), as well as a cooling of several hundred K in plasma temperature resulting from the reduction of solar extreme ultraviolet (EUV) heating (e.g., Goncharenko et al., 2018; MacPherson et al., 2000). Moreover, the additional effects of solar eclipse include the enhanced downward plasma diffusion from the plasmasphere due to the reduction in the plasma equilibrium scale height and F region density (Huba & Drob, 2017; Wang et al., 2019), the modified neutral dynamics and associated electrodynamics in response to the eclipse-induced atmospheric cooling and composition changes (C.-H. Chen et al., 2019; Harding et al., 2018; St.-Maurice et al., 2011), as well as atmospheric bow waves and traveling ionospheric disturbances (TIDs) (e.g., Chimonas, 1970; Liu et al., 2011; Mrak et al., 2018, 2022; Nayak & Yiğit, 2018; Sun et al., 2018; Zhang et al., 2017). Overall, the ionospheric response during a solar eclipse can be notably intricate due to the interplay of these dynamic photo-chemical, ambipolar diffusion, neutral wind, and electric field processes. Recently, significant improvements in the sensitivity and spatial-temporal resolution of observation techniques have yielded updated and more detailed insights into the ionospheric response to the influence of solar eclipse events. For example, studies of the Great American Solar Eclipse on 21 August 2017 have considerably benefited from the extensive coverage and significantly improved accuracy of various observational instruments, especially the dense ground-based GNSS receivers over the continental US (e.g., Cherniak & Zakharenkova, 2018; Coster et al., 2017; Zhang et al., 2017, 2021).

Although substantial progress has been made in prior studies of eclipses, some crucial issues still require further investigation as follows:

1. Different ionospheric responses to a solar eclipse at different latitudes. An eclipse event can occur at mid-to-high latitudes or at equatorial-to-low latitudes, and the eclipse-induced ionospheric variation can exhibit considerable latitudinal variation. The mid-latitude ionospheric plasma behavior can be largely controlled by plasma diffusion, while the equatorial and low-latitude ionospheric plasma are predominantly governed by the fountain effect of electrodynamics processes. For example, Le et al. (2009) analyzed the latitudinal dependence of ionospheric TEC and F2-layer peak density (NmF2) through multi-event comparison and numerical simulations, which showed that the eclipse effects are generally smaller at lower latitudes. However, each eclipse has its own characteristics with unique spatial/temporal coverage, and the background ionosphere-thermosphere conditions in each eclipse can be quite different. This could potentially introduce variability into the inter-eclipse analysis when attributing different ionospheric responses in different eclipses to their latitudinal variances. Therefore, from an observational point of view, it pertains a very unique value to investigate the ionospheric variations at different latitudes within a single eclipse event, particularly if the eclipse path traverses both the mid-latitude and equatorial/low-latitude regions in non-ocean areas with relatively good data coverage. This will provide key information for a more complete understanding of eclipse-induced latitudinal variation in ionospheric response.
2. Three-dimensional (3-D) ionospheric electron density variation during an eclipse, especially in the F region. In addition to the 2-D horizontal structure in GNSS TEC, notable changes in the ionosphere caused by a solar eclipse are equally distinct in the vertical domain as well (Goncharenko et al., 2018; Reinisch et al., 2018). In particular, the ionospheric F region response to a solar eclipse can be quite complicated, arising from multiple physical pathways associated with E-F region coupling through chemical processes, efficient plasma diffusion processes, eclipse-induced changes in neutral winds and composition and related ionosphere-thermosphere coupling, eclipse-induced electrodynamical processes, as well as the related plasma pressure gradient changes linking the F2 peak region to the topside ionosphere and even leading to the inter-hemispheric coupling, (e.g., Evans, 1965; Huba & Drob, 2017; Le et al., 2020; MacPherson et al., 2000; Rishbeth, 1968; Wang et al., 2019; Zhang et al., 2021). Thus, the F region electron density during an eclipse can either decrease or increase, occurring immediately or with a delay of tens of minutes following the progression of the eclipse. Because of the challenges in characterizing and understanding these phenomena and processes, investigating eclipse effects in the ionospheric F region remains some of the frontier areas in eclipse-related upper atmospheric studies. By examining the 3-D variations in ionospheric electron density, we can enhance the comprehension of the multi-dimensional alterations in the ionosphere during an eclipse, thereby advancing

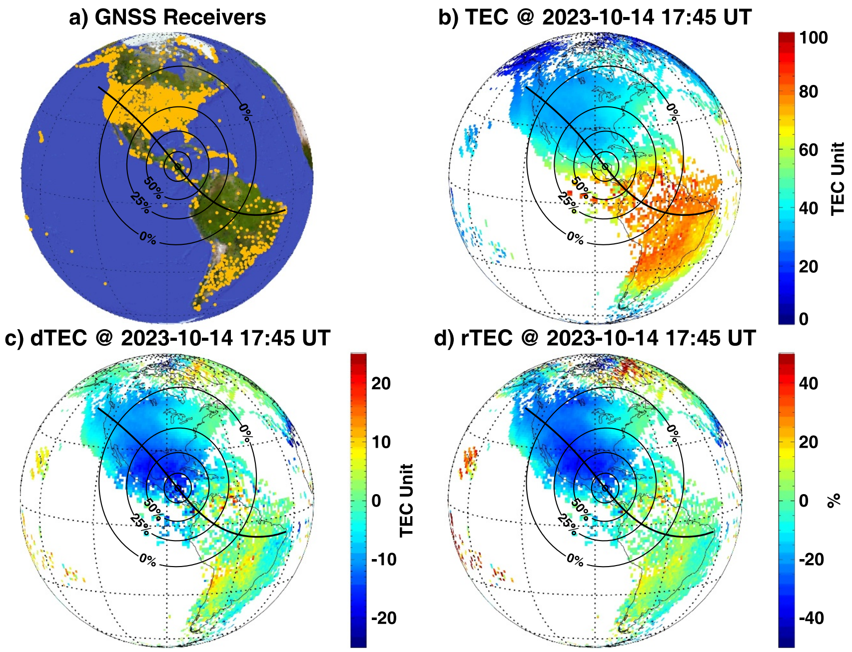

Figure 1. (a) GNSS receivers distribution over the American sector. (b–d) TEC, delta TEC (dTEC), and relative delta TEC (rTEC) maps at 17:45 UT on 14 October 2023. The annular solar eclipse path and the 0%, 25%, 50%, 75%, and 90% obscuration lines at 17:45 UT are also plotted in each panel.

the current understanding of the mechanisms that drive these changes (Aa, Forsythe, et al., 2023). Recently, some pioneering works have been conducted to reconstruct the 3-D ionospheric structure during the eclipse utilizing data assimilation or tomography technique (Aa, Zhang, et al., 2023; C. H. Chen et al., 2022; He et al., 2018; Lin et al., 2023).

On 14 October 2013, an annular solar eclipse passed across the North, Central, and South America from mid-latitude to equatorial regions, with the eclipse's path primarily traversing over the inland or coastal area with an unprecedented coverage of dense GNSS observation network of ~4,000 receivers. This event presented a valuable opportunity for exploring the eclipse-induced ionospheric effects at various latitudes, longitudes, and altitudes, considering the GNSS-based experimental technique has been proven capable of offering continuous and precise measurements of ionospheric changes in detail. In this paper, we report early multi-instrument observational results for this eclipse event encompassing two major areas of focus. First, we present a comprehensive analysis of the 2-D ionospheric TEC variation during this eclipse, derived from dense ground-based GNSS observations. Second, we use a recently developed new TEC-based ionospheric data assimilation system (TIDAS, Aa et al., 2022) to reconstruct and investigate the 3-D regional ionospheric electron density variations over the continental US during the eclipse. The observational and data assimilation analysis of ionospheric response motivates this study to further address aforementioned issues and to advance the current understanding of eclipse-induced ionospheric variations and underlying mechanisms.

2. Data Sets and Methodology

Ground-based GNSS TEC data is routinely generated and distributed via the Madrigal distributed data system that was developed at the Haystack Observatory of the Massachusetts Institute of Technology utilizing dense worldwide networks of ~5,000 GNSS receivers (Rideout & Coster, 2006; Vierinen et al., 2016). Figure 1a shows the distribution of ground-based GNSS receivers, demonstrating dense data coverage in the American sector through which the eclipse path transited. The gridded TEC maps were produced by averaging and binning all GNSS-derived TEC values into cells of 1° × 1° in geographic latitude and longitude at 5-min intervals. To examine the ionospheric variations induced by the eclipse, we compute the delta TEC values for the eclipse day by subtracting background reference TEC values. Here the reference TEC values are calculated as the 2-day average from pre-eclipse (October 12) and post-eclipse (October 15) days both under quiet geomagnetic conditions

(Kp < 2). October 13 was not used for reference since there were some unsettled geomagnetic activity with Kp reaching 3–4. We note that the solar activity was modest during the eclipse day with only few C-class flares, and no geospace storms occurred.

TIDAS is a novel TEC-based regional ionospheric data assimilation system, which employs a hybrid Ensemble-Variational method to assimilate a wide range of ionospheric observations from ground-based and space-borne TEC/Ne data, encompassing line-of-sight TEC data, radio occultation Ne data from COSMIC-I/II satellite, altimeter TEC measurements above the ocean from Jason satellite, and Ne measurements from the Millstone Hill incoherent scatter radar when data is available (Aa et al., 2022). TIDAS can produce high-resolution, time-evolving 3-D maps of ionospheric electron density across the continental US and adjacent regions, with a spatial-temporal resolution of 1° × 1° in latitude and longitude, 20 km in altitude, and a 5-min time cadence. The successful utilization of the TIDAS system to reconstruct 3-D ionospheric Ne during the 2017 Great American Solar Eclipse has been demonstrated and validated by Aa, Zhang, et al. (2023). For a more detailed description of the TIDAS algorithms, readers may refer to Aa et al. (2022, 2024). To further examine eclipse-induced ionospheric changes and to verify TIDAS results, we will also analyze electron density profiles and relevant F2-layer peak height parameters obtained from ionosonde measurements. In addition, we use in situ Ne measurements from the polar-orbiting Swarm A (~450 km) and B (~510 km) satellites.

3. Results

3.1. 2-D TEC Variations

Figure 1a displays a map of the annular solar eclipse path and the distribution of GNSS receivers on 14 October 2023. The solar eclipse started at ~15:05 UT over the Pacific Ocean near US west coast and ended at ~20:55 UT over the Atlantic near the east coast of South America. Figure 1b shows a TEC map at 17:45 UT with a superimposed eclipse path and different obscuration lines. As can be seen, the dense GNSS network is ideally positioned in the American sector to track the TEC variation during the eclipse with obscuration larger than 25%. Figures 1c and 1d show the corresponding delta TEC (dTEC) map in TEC units and relative delta TEC (rTEC) map as a percentage of background reference at 17:45 UT, respectively. A significant TEC reduction of 15–25 TEC units (25%–45%) can be seen in the vicinity of the eclipse shadow zone, especially in the trailing side over the North American region. At this time step, the region experiencing the maximum TEC reduction was observed near the Gulf of Mexico, approximately located between 50% and 75% obscuration lines to the northwest of the center of totality. This demonstrates that the ionospheric TEC decrease is not a simple linear function of solar obscuration with respect to the totality path but is more severe with a certain time delay in the trailing area than the leading area of the eclipse, which will be further analyzed in below.

To further demonstrate the temporal-spatial evolution of ionospheric TEC variations during the eclipse, Figure 2 depicts the dTEC maps with 30-min intervals between 15:00 and 22:00 UT on 14 October 2023. Figure 2a displays the pre-eclipse conditions at 15:00 UT, with some slight dTEC fluctuations of ±3 TECU in the North American sector. Figures 2b and 2c depict the subsequent two time steps, showing that the penumbral shadow rapidly emerged from behind the morning terminator and covered a large portion of the North American sector. The TEC began to decrease under the eclipse shadow, with approximate depletion of 5–10 TECU (10%–20%) over the continental US within the solar obscuration zone of 25%–50%. Moreover, Figures 2d–2g display the following evolution of dTEC maps in response to the solar eclipse until 18 UT, with the annular eclipse zone of ≥90% obscuration level passing over the North and Central America. As can be seen, the TEC values showed a substantial reduction of 15–25 TECU (25%–45%) over the continental US and Central America. The most notable TEC depletion occurred within the area of the 25% obscuration in the trailing region of the eclipse, with an approximate time lag of 30–60 min between the peak TEC depletion and the maximum eclipse obscuration.

Figures 2h–2l show the dTEC variation between 18:30 UT and 20:30 UT, when the annular eclipse passed across the South American sector within the equatorial region. The equatorial TEC depletion in the vicinity of the annular eclipse path was about 10–20 TECU (15%–25%), which is smaller than that of the North and Central America in the middle and low latitudes as previously mentioned. This demonstrates that the eclipse-induced ionospheric TEC response has a latitudinal dependence, with the TEC reduction being generally smaller in the lower latitudes than mid-latitudes, which is consistent with that indicated in the Le et al. (2009). During this time period, the North and Central America entered into the post-eclipse phase, and the TEC gradually recovered into its pre-eclipse levels in ~3 hr after the end of local eclipse. Furthermore, Figures 2m–2o display the dTEC

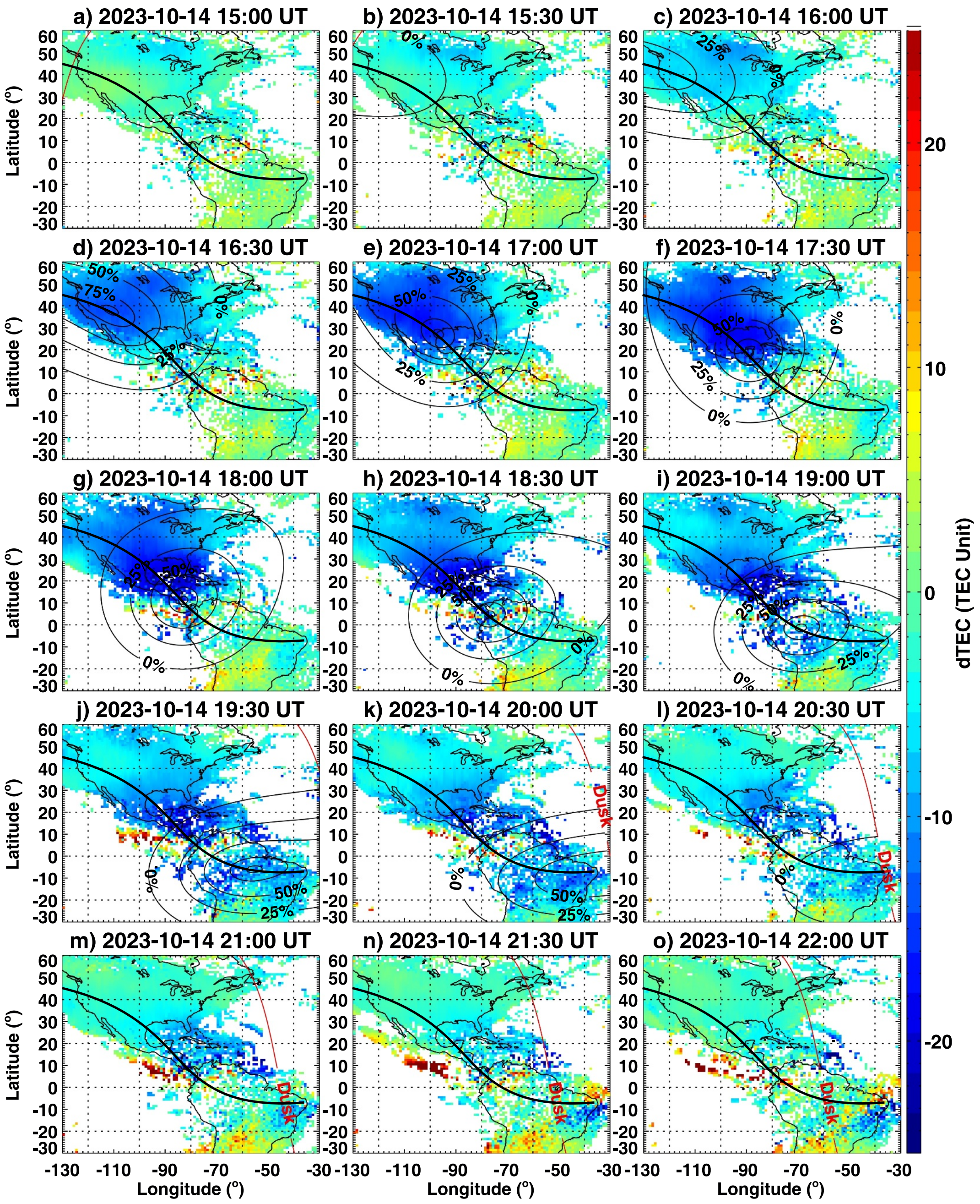

Figure 2. (a–o) 2-D delta TEC maps with 30-min interval during 15:00–22:00 UT on 14 October 2023. The annular eclipse path and different solar obscuration zones (0%, 25%, 50%, 75%, and 90%) are shown. The solar terminator is marked with a red curve.

evolution during 21:00–22:00 UT when the South American sector also transitioned into the post-eclipse phase. As can be seen, the TEC recovery was relative faster in the equatorial region than that of higher latitudes, which recovered into reference levels in ~1 hr and exhibited some slight post-eclipse enhancement of several TECU. In contrast, the mid-latitude TEC variation exhibited a different pattern with a much longer recovery time and displaying no significant post-eclipse enhancement. The complete set of TEC and delta TEC maps with a 5-min interval from 15 to 24 UT on 14 October 2023 are available in Movie S1.

To better analyze the latitudinal and longitudinal effects of ionospheric TEC changes during the eclipse, Figures 3a–3f show the zonal slices of delta TEC (dTEC) and relative delta TEC (rTEC) keograms as a function of

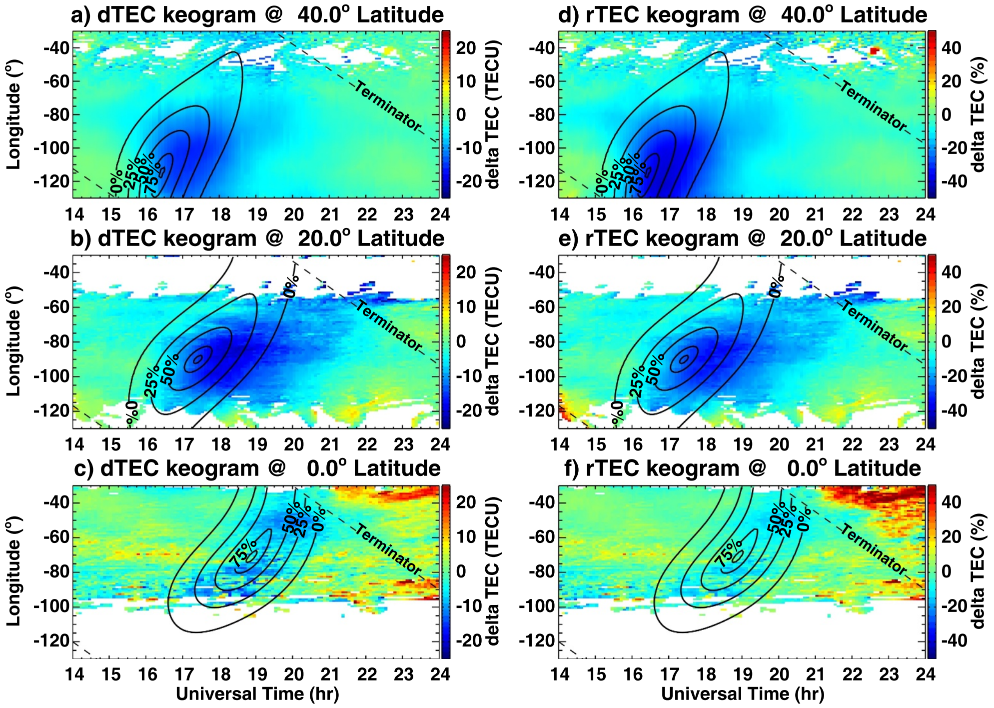

Figure 3. The delta TEC (a–c) and relative delta TEC (d–f) keograms as a function of longitude and time at different latitudes (40°, 20°, and 0°). Different solar obscuration degree (0%, 25%, 50%, 75%, and 90%) and solar terminator are also shown.

longitude and time at three different latitudes, respectively. The eclipse-induced ionospheric TEC reduction can be clearly observed at each panel but with notable latitudinal differences in magnitudes. At the mid-latitude location of 40° (Figures 3a and 3d), the TEC depletion mainly occurred in the continental US longitudes between 70°W–130° and 16–18 UT, with the depletion level being about 10–15 TECU (20%–40%) within the 25% obscuration zone. The TEC values gradually recovered to the pre-eclipse levels in ∼2–3 hr after the local eclipse end with no post-eclipse enhancements. Similarly, at 20° latitude (Figures 3b and 3e), the TEC depletion was about 10–20 TECU (20%–45%) between 60°W–120°W and 17–20 UT. Again, the TEC values returned to their pre-eclipse levels in 2–3 hr after the local eclipse ended, without noticeable post-eclipse enhancements. However, the equatorial ionospheric TEC responses at 0° latitude (Figures 3b and 3e) exhibit a notable difference. The reduction in TEC induced by the eclipse was merely 5–10 TECU (10%–15%) within the 25% obscuration zone, which is considerably smaller than that at higher latitudes. Moreover, the TEC values quickly recovered to pre-eclipse levels in ∼1 hr, followed by a moderate post-eclipse enhancement of 10%–20% during 22–24 UT. This is different from that at higher latitudes with no clear post-eclipse enhancements.

To further investigate the latitudinal effect of eclipse-induced ionosperic TEC variation, Figures 4a and 4b show the dTEC and rTEC keograms along the annular eclipse path as a function of latitude and time, respectively. Although the TEC reduction and recovery can be observed at all latitudes during the eclipse, it exhibits a pronounced latitudinal difference: there was a more substantial TEC decrease associated with a longer recovery period near but to the poleward side of northern EIA crest (10°N–45°N) than that at the equatorial and low-latitude region (5°S–10°N). Specifically, Figure 4c displays the latitudinal profiles of the maximum TEC reduction within the annular eclipse zone. As can be seen, the averaged TEC reduction in the latitude range of 10°N–40°N was about 13–23 TECU (25%–42%). In particular, the dTEC showed a clear decreasing trend with more deepened depletion in terms of decreasing latitudes, which reached a maximum depletion of 23 TECU at 13°N. However, at the equatorial and low-latitude region between 5°S and 10°N, the averaged TEC reduction was about 8–17 TECU (10%–25%), comparatively smaller than that at higher latitudes. Furthermore, the previously intensified trend of depletion was completely reversed with the TEC reduction being drastically weakened toward lower latitudes. Notably, the minimum TEC depletion of 8 TECU (∼10%)

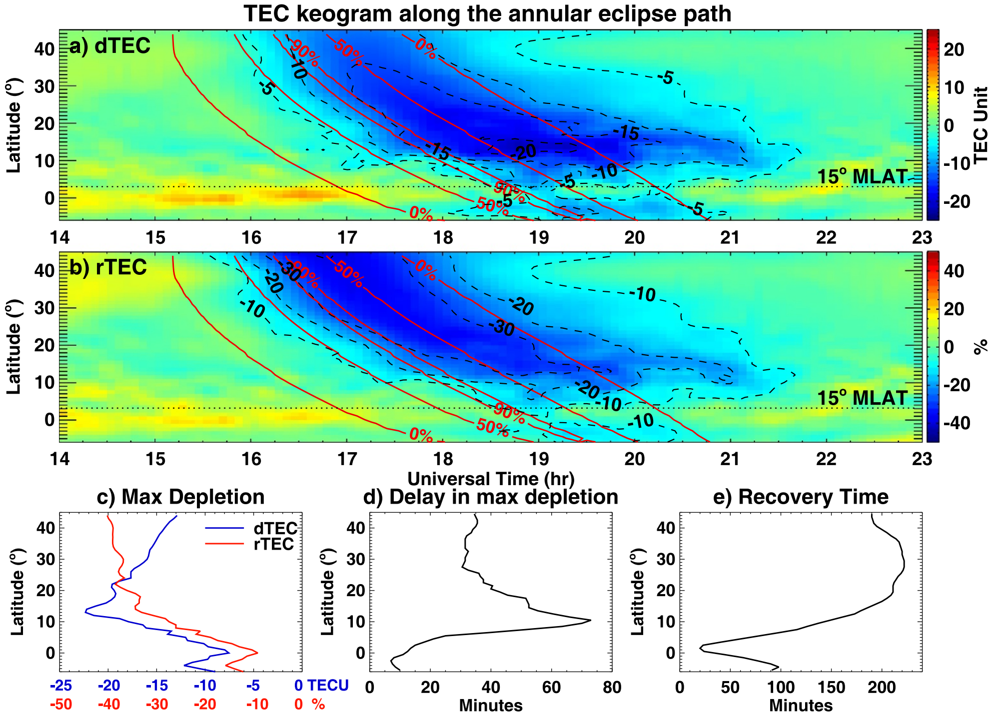

Figure 4. (a and b) The delta TEC and relative delta TEC keograms along the annular eclipse path as a function of latitude and time. Different solar obscuration zones (0%, 50%, and 90%) are marked with red curves. Geomagnetic 15° latitude is marked with a dotted line. (c) Maximum dTEC and rTEC reduction for different latitudes. (d) Time delay between maximum solar obscuration and maximum TEC depletion. (e) Time of TEC recovery to pre-eclipse levels.

occurred at ~0° latitude, approximately in the vicinity of northern EIA crest though the background TEC values were quite large.

Figure 4d shows the time delay between the maximum solar obscuration and the most significant TEC depletion as a function of latitude. In the mid-latitude region of 25°N–45°N, the time delay was about 30–35 min. It gradually increased to 60–70 min between 10°N and 15°N and then drastically decreased to 5–20 min between 5°S and 5°N. This latitudinal dependency of time delay generally correlates positively with the latitudinal variation of the delta TEC (i.e., a larger TEC depletion corresponds to a longer time delay). Moreover, Figure 4e shows the latitudinal variation of TEC recovery time to pre-eclipse levels. A notably longer recovery time period of 3–4 hr was observed between 15°N and 45°N. In contrast, the fastest recovery time, ranging from 20 to 40 min, was recorded in the vicinity of the northern EIA crest at ~0°–4° latitude (15° MLAT). As previously mentioned, this latitudinal location also experienced the least TEC reduction and encountered the shortest time delay. We will further analyze such a substantial latitudinal difference in TEC responses in the Discussion section.

3.2. 3-D Ionospheric Electron Density Variations

Figures 5a–5d depict the delta TEC maps over the continental US and adjacent areas at four UT intervals during 15:15–18:15 UT on 14 October 2023. This period corresponds to the passage of the annular eclipse across continental US from the west coast to the gulf of Mexico. Black stars mark the location of four ionosondes: Pt Arguello (34.8°N, 120.5°W, maximum obscuration: 70%), Boulder (40.0°N, 105.3°W, maximum obscuration: 79%), Austin (30.4°N, 97.7°W, maximum obscuration: 89%), and Eglin (30.5°N, 86.5°W, maximum obscuration: 63%). Figures 5e–5l show the electron density profiles observed by these four ionosondes during 14–24 UT on the eclipse day and reference day, respectively. Notably, the Ne profiles at all these ionosondes exhibit a distinct bite-out phenomenon during the eclipse period, particularly between 200 and 400 km in the ionospheric F-region. The reduction in electron density occurred shortly after the eclipse commenced, reaching its maximum depletion around 30–40 min after the local maximum obscuration and gradually recovered to pre-eclipse levels after the ending of local eclipse. However, it is important to note that the topside Ne profile above the F2 peak is derived

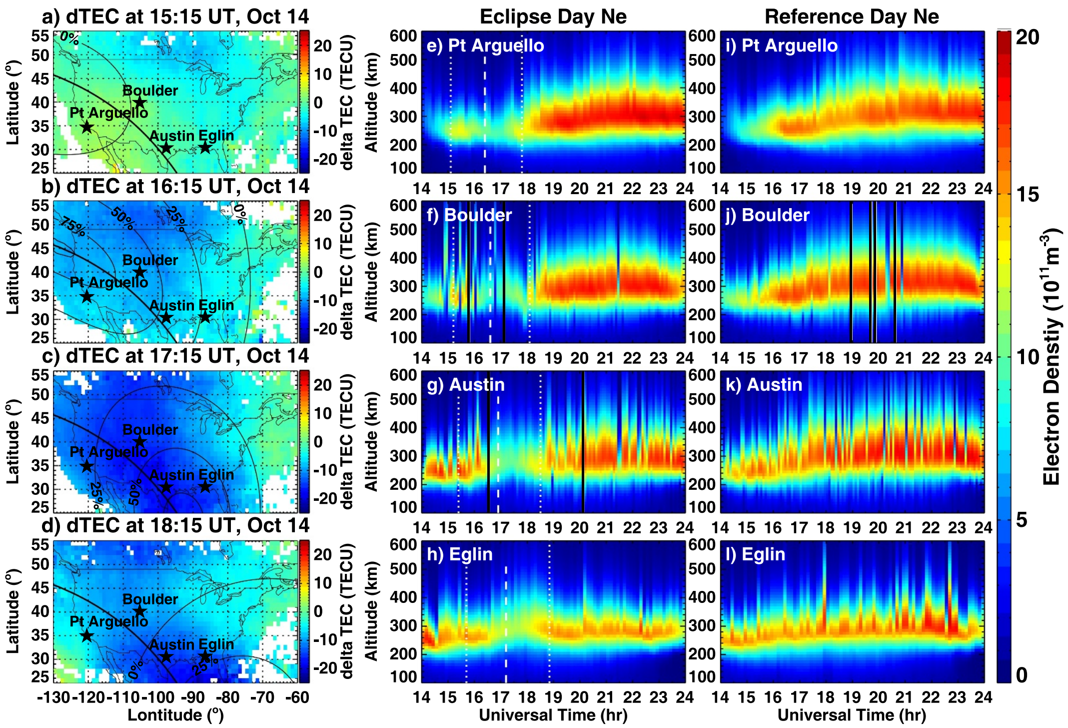

Figure 5. (a–d) Delta TEC maps over the continental US and adjacent areas at four UT intervals between 15:15 and 18:15 UT on 14 October 2023. The locations of four ionosondes are marked with stars. The annular solar eclipse path and the 0%, 25%, 50%, 75%, and 90% obscuration lines are plotted in each panel. (e–l) Comparison of ionosonde electron density profiles between 14 and 24 UT on the eclipse day (October 14) and the reference day (October 12), respectively. The local eclipse start, maximum, and end times are marked with vertical white lines.

under the assumption of an α-Chapman shape of plasma distribution (Reinisch & Huang, 2001). Furthermore, these automatic ionosonde measurements exhibit sporadic data gaps with some large uncertainties, making them more suitable for a preliminary evaluation of the eclipse effect. Thus, we will employ the TIDAS data assimilation technique to conduct an in-depth analysis of the ionospheric electron density response.

Figures 6a–6h show the TIDAS-reanalyzed electron density profiles at four ionosondes during 14–24 UT on the eclipse day (October 14) and reference day (average of October 12 and 15), respectively. Comparison of these Ne profiles with those shown in Figure 5 reveals a notable agreement between the TIDAS data assimilation results and the ionosonde observations. The data-driven TIDAS results possess the advantage of effectively reproducing the altitude-resolved electron density variation during the eclipse with no sporadic data gaps or outliers. Figures 6i–6p illustrate the corresponding delta electron density (dNe) and relative delta Ne profiles at those ionosonde locations. These profiles reveal a noticeable Ne reduction of 3–7 × 10^{11} el/m^3 (~30%–50%) across the bottomside and topside ionosphere, which occurred shortly after the onset of the local eclipse, reaching the largest depletion in the ionospheric F2 region between 250 and 350 km approximately 30–40 min after the local maximum obscuration. The reduction in Ne exhibits an altitude-dependent feature, with a more pronounced depletion observed around the ionospheric F2-layer peak region, which is consistent with that of 2017 Great American solar eclipse as observed by incoherent scatter radar (Goncharenko et al., 2018) or reconstructed using tomography technique (C. H. Chen et al., 2022). Specifically, the maximum Ne reduction was 5.7 × 10^{11} el/m^3 (~44%) at ~260 km over Pt Arguello, 6.5 × 10^{11} el/m^3 (~46%) at ~280 km over Boulder, 6.8 × 10^{11} el/m^3 (~42%) at ~300 km over Austin, and 5.9 × 10^{11} el/m^3 (~35%) at ~300 km over Eglin. After the ending of the local eclipse, the ionospheric electron density gradually recovered to pre-eclipse levels in 3–4 hr. The recovery process demonstrates an altitude-dependent characteristic, where Ne near the F2-region peak height (250–350 km) exhibited a relatively slower recovery with approximately ~1 hr lag compared to those at lower and higher altitudes. We will further analyze these altitude-dependent features in the discussion section.

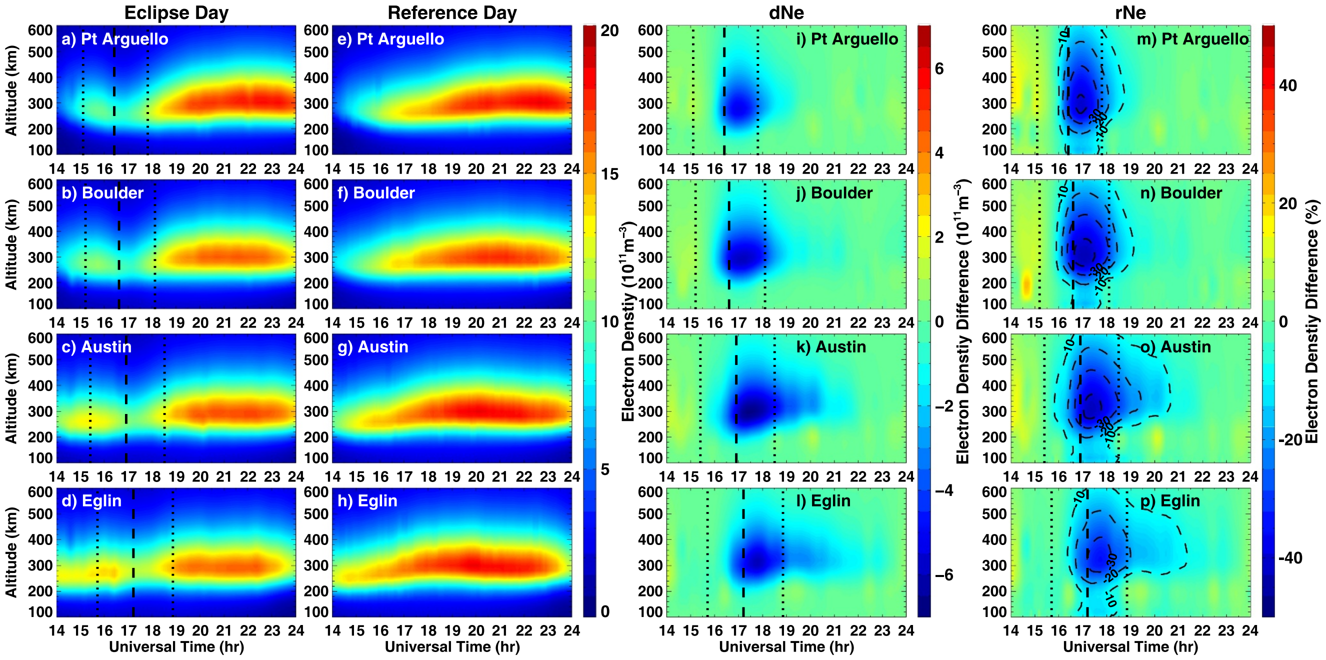

Figure 6. (a–h) Comparison of TIDAS-reanalyzed electron density profiles at four ionosondes locations during 14–24 UT on the eclipse day (October 14) and the reference day (average of October 12 and 15), respectively. (i–p) The delta electron density (dNe) and relative delta Ne between the eclipse day and reference day. The local eclipse start, maximum, and end times are marked with vertical lines.

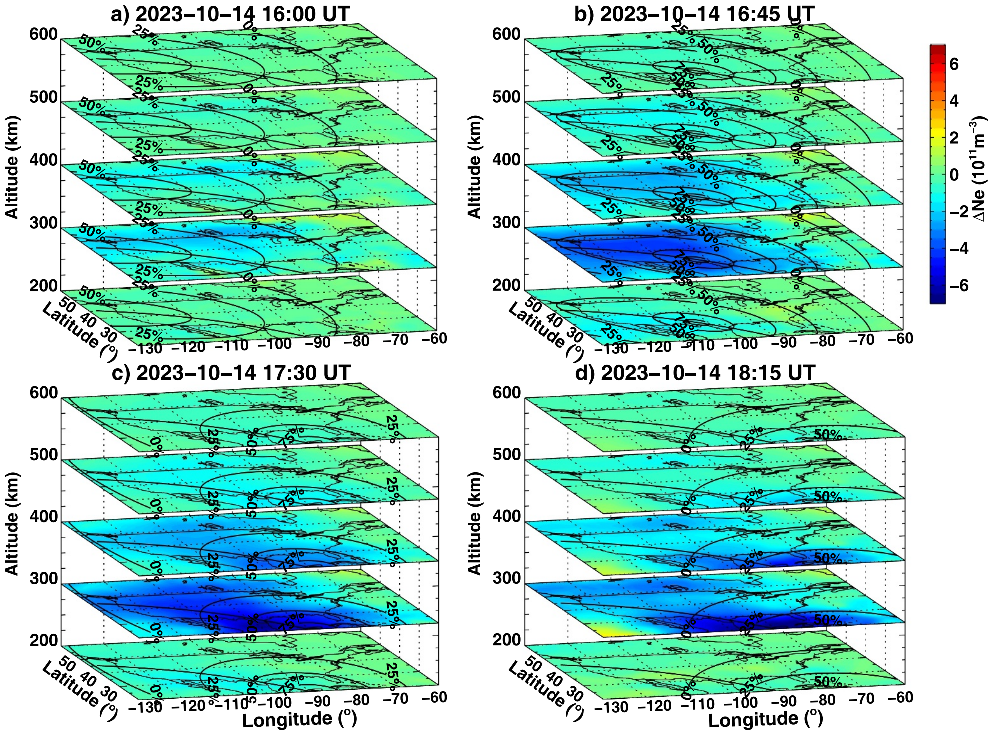

Figure 7. (a–d) 3-D distribution of the TIDAS-reconstructed delta Ne maps at four UT intervals between 16:00 and 18:15 UT on 14 October 2023. The annular eclipse path and different obscuration zones of 0%, 25%, 50%, 75%, and 90% are plotted.

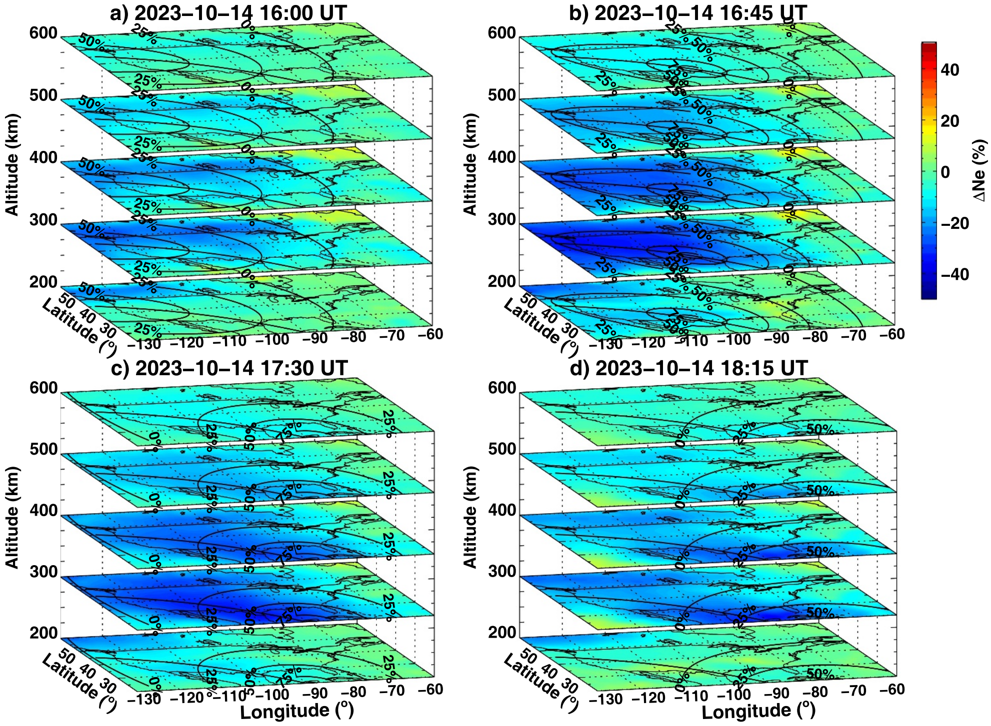

Figure 8. (a–d) The same as Figure 7, but for percentage delta Ne maps.

To offer a more comprehensive illustration of the time-evolving 3-D ionospheric electron density variation during the annular eclipse, Figures 7 and 8 present examples of the horizontal distribution of TIDAS-reanalyzed absolute and percentage delta Ne maps over the continental US and adjacent regions between 200 and 600 km at four UT intervals on 14 October 2023. These images demonstrate that the ionospheric electron density experienced a noticeable reduction across all altitudes during the eclipse, which traveled across the continental US from the west coast to the Gulf of Mexico in alignment with the passage of the annular eclipse. Within the 25% obscuration zone, the reduction in electron density ranged between 3 and 7×10^{11} el/m^3 (~30%–50%), with the most substantial depletion observed at around 300 km near the F2-layer peak height.

Figure 9 displays the spatial-temporal evolution of the TIDAS-reanalyzed delta NmF2 (F2-layer peak density) and delta hmF2 (F2-layer peak height) maps over the continental US and adjacent regions at four UT intervals on 14 October 2023. With respect to the advancement of the annular eclipse, the NmF2 maps reveal a corresponding notable eclipse-induced depletion ranging from 30% to 50%. In comparison, the variation of hmF2 was not as significant as that of NmF2. Figures 9a and 9b show that hmF2 shows some slight perturbations with small enhancement at the leading edge of the annular eclipse but some decrease in the vicinity of the annular eclipse center. Moreover, Figures 9a and 9b display that there was a moderate decrease in hmF2 by 20–30 km at the trailing edge of the eclipse (i.e., 80–100°W, 20–40°N) within 25% of the solar obscuration. The minor perturbations may correspond to the eclipse-induced TIDs. The decrease in hmF2 is attributed to the eclipse-induced depletion of ionospheric F-region before the ionosphere begins to rebuild from lower altitudes. This finding aligns with the descending layer observed after maximum obscuration in the ionosonde results, as shown in Figure 5.

To further validate the variations in the ionospheric peak density and peak height reanalyzed by TIDAS data assimilation, Figure 10 illustrates the NmF2 and hmF2 measurements obtained from the aforementioned four ionosondes. Due to the eclipse-induced loss in photo-ionization, the NmF2 exhibits a prominent reduction of 3–7×10^{11} el/m^3 at these ionosondes during the eclipse, with the maximum depletion of 45% at Pt Arguello, 47% at Boulder, 41% at Austin, and 33% at Eglin, which occurred 20–30 min after the maximum local obscuration. The levels of these reductions magnitudes are generally consistent with those of the TIDAS data assimilation results shown in Figures 6 and 9. Regarding the hmF2 variation during the eclipse day (Figures 10e–10h), there was no

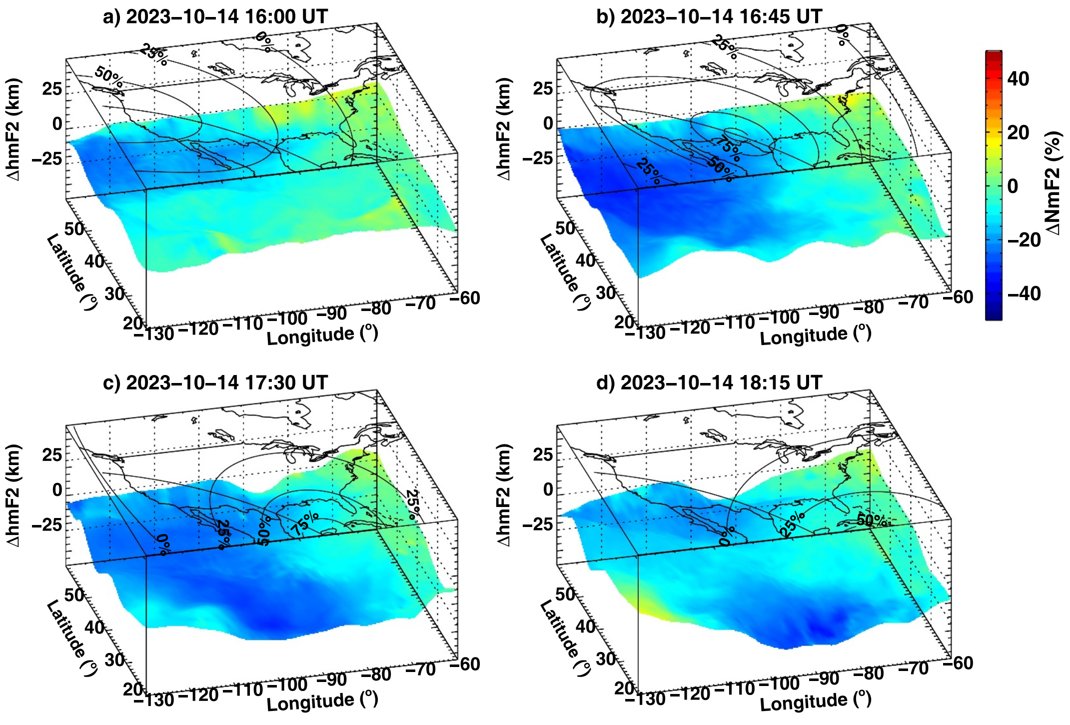

Figure 9. (a–d) TIDAS-reanalyzed delta NmF2 (F2-layer peak density, color-coded) and delta hmF2 (F2-layer peak height) variations over continental US and adjacent areas at four UTs between 16:00 and 18:15 UT on 14 October 2023. The annular eclipse path and different obscuration zones of 0%, 25%, 50%, 75%, and 90% are also marked.

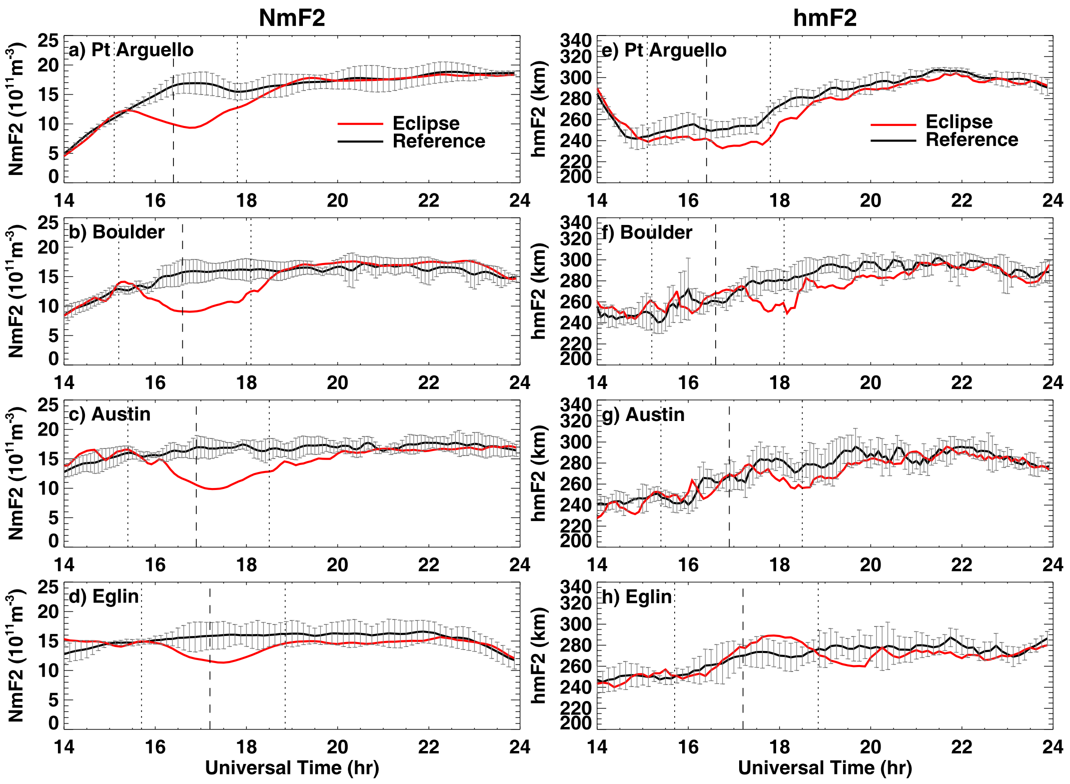

Figure 10. Ionosonde NmF2 (a–d) and hmF2 (e–h) measurements during the eclipse and reference periods. The local eclipse start, maximum, and end times are marked with vertical lines.

significant deviations from the uncertainty envelope during the leading phase of the eclipse, though some slight increase of 20 km can be observed in Eglin. However, the hmF2 experienced a somewhat decreasing trend during the recovery phase of the eclipse, registering 20–30 km lower than the reference values shortly after the ending of the local eclipse. Such a variation trend of the peak height is similar to that reported by Reinisch et al. (2018) and agrees well with the reanalyzed results given by TIDAS data assimilation in Figure 9.

4. Discussion

The 2-D TEC responses during this annular eclipse exhibited distinct latitudinal differences: the midlatitude ionosphere was characterized by a more substantial TEC decrease of 13–23 TECU (25%–40%) associated with a longer time delay (30–70 min) and an extended recovery time (3–4 hr), while the equatorial and low-latitude ionosphere showed a smaller TEC reduction of 8–17 TECU (10%–25%), a shorter time delay (5–20 min), and a much faster recovery time (20–50 min). The minimal eclipse effect was observed near the northern EIA crest region, with a merely ∼10% TEC reduction and a quick recovery in 20 min. These substantial latitudinal differences could be collectively attributed to the following reasons.

(1) Different prevailing processes at different latitudinal regions. It is known that the midlatitude ionospheric plasma behavior can be largely controlled by photo-chemical and diffusion processes, while the equatorial and low-latitude ionosphere are subject to strong fountain effect of electrodynamics processes. In the 15°N–40°N latitudes beyond the northern EIA crest, our results show that the maximum delta TEC reduction and time delay with respect to largest solar obscuration were more intense at lower latitudes than at higher latitudes. This latitudinal dependence is commonly ascribed to higher background neutral concentrations that are associated with larger ionospheric loss coefficients at lower latitudes (Ding et al., 2010; Le et al., 2009). In contrast, this latitudinal dependence was completely reversed for the equatorial anomalies region: the eclipse effect significantly weakened with decreasing latitude until around 0° (Figures 4c–4e). Earlier studies have indicated that the F2-layer and topside ionospheric variation in the equatorial anomalies region is controlled more by fountain effect than by local solar radiation during the eclipse (Cheng et al., 1992; Tsai & Liu, 1999). Hence, the ambipolar diffusion associated with the equatorial fountain effect can effectively mitigate the eclipse-induced electron density reduction around EIA crests, causing the least TEC depletion and the fast recovery therein.

(2) Local time dependence of the eclipse effects. The latitudinal variation of eclipse path was also intertwined with local time changes. In the mid-latitude regions over the continental US, the eclipse began in the morning when the ionosphere was still in the process of formation due to the enhanced solar EUV illumination. Therefore, the photo-chemical processes would consequently take on a more dominant role than transport processes (Rishbeth et al., 1995). On the contrary, in the equatorial and low-latitude region over the South American sector, the eclipse commenced in the local afternoon when the daytime ionosphere was already in a well-established balance between photochemical and dynamical processes thus $dN/dt \sim 0$. Therefore, the eclipse-induced inhibition in photo-ionization would result in a more significant TEC reduction in the local morning sector compared to the afternoon eclipse. This is similar to those occurred over the equatorial region during the 26 December 2019 annular eclipse (Aa et al., 2020).

(3) Eclipse-induced thermospheric wind and ambipolar diffusion effect. Numerous studies have indicated that the thermospheric cooling within the eclipse shadow could induce low-pressure systems and trigger substantial neutral wind convergence toward the eclipse region (e.g., Choudhary et al., 2011; Cnossen et al., 2019; Müller-Wodarg et al., 1998; St.-Maurice et al., 2011; Yan et al., 2021). When the annular eclipse traversed across the equatorial anomalies region during 18:30–20:00 UT on October 14, the disturbed meridional wind component ought to be southward in the poleward side of northern EIA crest. This equatorward disturbance wind would raise plasma to a higher altitude with slower recombination rate and alleviate the eclipse-induced depletion, especially near the northern EIA crest. On the other hand, the eclipse-induced electron temperature and electron density reduction will cause low plasma pressure near the totality, resulting in a large plasma pressure gradient that drove the plasma into the region (e.g., Zhang et al., 2021). The combination of this eclipse-induced plasma pressure gradient and fountain-related plasma pressure gradient in the equatorial anomalies region would effectively increase the poleward ambipolar diffusion into the EIA crest region. This positive effect tend to balance out the net decrease in electron density caused by the photochemical effect (Dang et al., 2020; Wang et al., 2019), thereby contributing to less TEC reduction and fast recovery in the vicinity of northern EIA crest as we

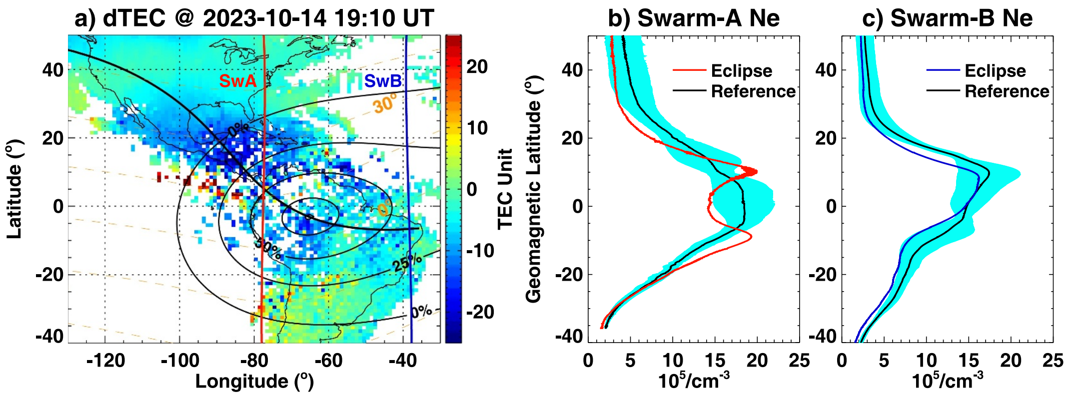

Figure 11. (a) Delta TEC map at 19:10 UT on 14 October 2023, overlapping with the Swarm A (red) and Swarm B (blue) orbits, respectively. The annular eclipse path and different obscuration zones of 0%, 25%, 50%, 75%, and 90% are also marked. The geomagnetic latitudes with 15° interval are marked by orange dashed lines. (b and c) Latitudinal variation of corresponding Swarm in situ Ne profiles.

observed. We note that there is currently no available daytime low-latitude thermospheric wind data for this eclipse event, and future modeling work is essential to enhance our understanding on this intricate latitudinal effect.

(4) Electrodynamic effect due to modification of the conductance. A solar eclipse is analogous to a rapid local sunset, triggering a quick decrease in conductance, particularly in the lower E region, due to the inhibition of ionization (Huba & Drob, 2017; Rishbeth, 1968). In the equatorial and low-latitude region, such a rapid eclipse-induced modification of conductance, combined with the curl-free requirement for the electric field, may lead to a considerable enhancement of the eastward zonal electric field and the upward E × B drift (Aa et al., 2020; G. Chen et al., 2011; Dear et al., 2020; Tsai & Liu, 1999; Tomás et al., 2007). Such an electrodynamic effect could amplify the equatorial fountain effect, mitigate the electron density reduction in the EIA crest region or even cause slight enhancement therein, as observed in Figure 2. Moreover, Figure 11 shows the solar obscuration distribution at 19:10 UT on the eclipse day, along with the corresponding paths of Swarm satellites and latitudinal Ne profiles. Swarm B, flying at 500 km, crossed the edge of eclipse zone with less than 25% obscuration, resulting in a Ne reduction of about 10%–20%. In contrast, Swarm A, flying at 450 km, traversed the 50%–75% obscuration zone in the equatorial and low-latitude region, merely 30–40 min after the annular eclipse had passed. In the midlatitude North American region, Swarm A encountered a density reduction of 20%–40%, consistent with that reconstructed by TIDAS. However, in the equatorial and low-latitude region, Swarm A experienced a noticeable equatorial trough and clear double-crests EIA structures during the eclipse day, consistent with the TEC results. This indicates that the equatorial fountain effect was enhanced even under the shadow of solar eclipse, lending support to the aforementioned electrodynamic effect. Future theoretical simulation studies on this eclipse event are needed to provide a more comprehensive understanding of this electrodynamic effect.

The 3-D variations in ionospheric electron density during the eclipse was effectively reconstructed using the TIDAS data assimilation system, incorporating crucial altitude information. TIDAS results demonstrate that the eclipse caused a significant electron density reduction of 30%–50% across the bottom and topside ionosphere, with the maximum depletion observed around the ionospheric F2-layer peak height between 250 and 350 km. TIDAS results also indicate that the subsequent recovery of electron density after the eclipse displays an altitude-dependent characteristic: the electron density near the F2-layer peak height demonstrates a comparatively slower recovery pace than those at lower and higher altitudes. For the ionosphere at lower altitudes, the relatively quick recovery of Ne therein can be attributed to the more immediate impact of changes in the photo-ionization rate on the photochemical equilibrium at these lower altitudes (Goncharenko et al., 2018). For the topside ionosphere at higher altitudes, the comparatively fast recovery of Ne therein can be attributed to the downward plasma diffusion due to the eclipse-induced reduction in plasma temperature and scale height, which leads to a replenishment of the electron density that is more pronounced at higher altitude above the F2-layer peak height (e.g., Evans, 1965).

5. Conclusions

This paper studies the 2-D ionospheric TEC responses and 3-D electron density variations during the annular solar eclipse on 14 October 2023, utilizing ground-based GNSS observations, a new TEC-based ionospheric data assimilation system (TIDAS), and ionosonde measurements. The analysis focuses on the latitudinal and altitudinal dependence of the eclipse-induced ionospheric responses, with the main results being summarized as follows.

1. Distinct latitudinal differences in the 2-D TEC responses were observed during this annular eclipse. In the midlatitude ionosphere, there was a more substantial TEC decrease of 25%–40%, accompanied by a longer time delay of 30–70 min and an extended recovery time of 3–4 hr. Conversely, the equatorial and low-latitude ionosphere exhibited a smaller TEC reduction of 10%–25%, a shorter time delay of 5–20 min, and a much faster recovery time of 20–50 min. The minimal eclipse effects were observed near the northern EIA crest region, with only a ∼10% TEC reduction and a rapid recovery within 20 min.
2. The TIDAS data assimilation system was used to reconstruct the 3-D ionospheric electron density variations during the eclipse over the continental US and adjacent regions, providing crucial altitude information that were in agreement with that estimated from ionosonde measurements. This effectively captured the essential characteristics of eclipse-induced electron density reduction and the subsequent recovery, which highlights intricate features with details in the 3-D domain.
3. The ionospheric electron density variation during the eclipse exhibited a noticeable altitude-dependent feature. The eclipse led to a substantial reduction in electron density, ranging from 30% to 50%, with the maximum depletion observed around the F2-layer peak height. The recovery in electron density after the eclipse demonstrates a relatively slower pace near the F2-layer peak height with ∼1 hr delay compared to that at lower and higher altitudes. Moreover, the ionospheric hmF2 exhibited perturbations with a slight rise at the leading edge of the eclipse, followed by a moderate decrease of 20–30 km after the maximum obscuration.

Data Availability Statement

GNSS TEC data products are provided through the Madrigal distributed data system by MIT Haystack Observatory (http://cedar.openmadrigal.org/). The ionosonde data are provided by the University of Massachusetts Lowell DIDB database of Global Ionospheric Radio Observatory (https://giro.uml.edu/didbase/scaled.php). Swarm data are provided by European Space Agency (https://swarm-diss.eo.esa.int/).

Acknowledgments

We acknowledge NSF awards AGS-1952737, AGS-2033787, AGS-2149698, PHY-2028125, and NSFC41974184, NASA support 80NSSC22K0171, 80NSSC21K1310, 80NSSC21K1775, 80NSSC19K0834, 80NSSC20K1785, and 80GSFC22CA011, AFOSR MURI Project FA9559-16-1-0364, and ONR Grants N00014-17-1-2186 and N00014-22-1-2284. Data for TEC processing is provided from the following organizations: UNAVCO, SOPAC, IGN (France), IGS, CDDIS, NGS, IBGE (Brazil), RAMSAC (Argentina), CORS (Panama), Arecibo Observatory, LISN, Topcon, CHAIN (Canada), CRS (Italy), SONEL, RENAG (New Zealand), GNSS Reference Networks, Finnish Meteorological Institute, and SWEPOS.

References

Aa, E., Forsythe, V. V., Zhang, S.-R., Wang, W., & Coster, A. J. (2023). Next-decade needs for 3-D ionosphere imaging. *Frontiers in Astronomy and Space Sciences*, *10*, 1186513. https://doi.org/10.3389/fspas.2023.1186513

Aa, E., Zhang, S.-R., Erickson, P. J., Goncharenko, L. P., Coster, A. J., Jonah, O. F., et al. (2020). Coordinated ground-based and space-borne observations of ionospheric response to the annular solar eclipse on 26 December 2019. *Journal of Geophysical Research: Space Physics*, *125*(11), e28296. https://doi.org/10.1029/2020JA028296

Aa, E., Zhang, S.-R., Erickson, P. J., Wang, W., & Coster, A. J. (2023). 3-D ionospheric electron density variations during the 2017 Great American solar eclipse: A revisit. *Atmosphere*, *14*(9), 1379. https://doi.org/10.3390/atmos14091379

Aa, E., Zhang, S.-R., Erickson, P. J., Wang, W., Coster, A. J., & Rideout, W. (2022). 3-D regional ionosphere imaging and SED reconstruction with a new TEC-based ionospheric data assimilation system (TIDAS). *Space Weather*, *20*(4), e2022SW003055. https://doi.org/10.1029/2022SW003055

Aa, E., Zhang, S.-R., Erickson, P. J., Wang, W., Coster, A. J., & Rideout, W. (2024). 3-D ionospheric imaging over the South American region with a new TEC-based ionospheric data assimilation system (TIDAS-SA). *Space Weather*, *22*(2), e2023SW003792. https://doi.org/10.1029/2023SW003792

Aa, E., Zhang, S.-R., Shen, H., Liu, S., & Li, J. (2021). Local and conjugate ionospheric total electron content variation during the 21 June 2020 solar eclipse. *Advances in Space Research*, *68*(8), 3435–3454. https://doi.org/10.1016/j.asr.2021.06.015

Afraimovich, E. L., Palamartchouk, K. S., Perevalova, N. P., Chernukhov, V. V., Lukhnev, A. V., & Zalutsky, V. T. (1998). Ionospheric effects of the solar eclipse of March 9, 1997, as deduced from GPS data. *Geophysical Research Letters*, *25*(4), 465–468. https://doi.org/10.1029/98GL00186

Aryal, S., Evans, J. S., Correira, J., Burns, A. G., Wang, W., Solomon, S. C., et al. (2020). First global-scale synoptic imaging of solar eclipse effects in the thermosphere. *Journal of Geophysical Research: Space Physics*, *125*(9), e27789. https://doi.org/10.1029/2020JA027789

Chen, C. H., Lin, C. C. H., Lee, C. J., Liu, J. Y., & Saito, A. (2022). Ionospheric responses on the 21 August 2017 solar eclipse by using three-dimensional GNSS tomography. *Earth Planets and Space*, *74*(1), 173. https://doi.org/10.1186/s40623-022-01734-y

Chen, C.-H., Lin, C.-H. C., & Matsuo, T. (2019). Ionospheric responses to the 21 August 2017 solar eclipse by using data assimilation approach. *Progress in Earth and Planetary Science*, *6*(1), 13. https://doi.org/10.1186/s40645-019-0263-4

Chen, G., Qi, H., Ning, B., Zhao, Z., Yao, M., Deng, Z., et al. (2013). Nighttime ionospheric enhancements induced by the occurrence of an evening solar eclipse. *Journal of Geophysical Research: Space Physics*, *118*(10), 6588–6596. https://doi.org/10.1002/jgra.50551

Chen, G., Zhao, Z., Ning, B., Deng, Z., Yang, G., Zhou, C., et al. (2011). Latitudinal dependence of the ionospheric response to solar eclipse of 15 January 2010. *Journal of Geophysical Research*, *116*(A6), A06301. https://doi.org/10.1029/2010JA016305

Cheng, K., Huang, Y.-N., & Chen, S.-W. (1992). Ionospheric effects of the solar eclipse of September 23, 1987, around the equatorial anomaly crest region. *Journal of Geophysical Research*, *97*(A1), 103–112. https://doi.org/10.1029/91JA02409

Cherniak, I., & Zakharenkova, I. (2018). Ionospheric total electron content response to the Great American solar eclipse of 21 August 2017. *Geophysical Research Letters*, *45*(3), 1199–1208. https://doi.org/10.1002/2017GL075989

Chimonas, G. (1970). Internal gravity-wave motions induced in the Earth's atmosphere by a solar eclipse. *Journal of Geophysical Research*, *75*(28), 5545–5551. https://doi.org/10.1029/JA075i028p05545

Choudhary, R. K., St. -Maurice, J. P., Ambili, K. M., Sunda, S., & Pathan, B. M. (2011). The impact of the January 15, 2010, annular solar eclipse on the equatorial and low latitude ionospheric densities. *Journal of Geophysical Research*, *116*(A9), A09309. https://doi.org/10.1029/2011JA016504

Cnossen, I., Ridley, A. J., Goncharenko, L. P., & Harding, B. J. (2019). The response of the ionosphere-thermosphere system to the 21 August 2017 solar eclipse. *Journal of Geophysical Research: Space Physics*, *124*(8), 7341–7355. https://doi.org/10.1029/2018JA026402

Coster, A. J., Goncharenko, L., Zhang, S.-R., Erickson, P. J., Rideout, W., & Vierinen, J. (2017). GNSS observations of ionospheric variations during the 21 August 2017 solar eclipse. *Geophysical Research Letters*, *44*(24), 12041–12048. https://doi.org/10.1002/2017GL075774

Dang, T., Lei, J., Wang, W., Yan, M., Ren, D., & Huang, F. (2020). Prediction of the thermospheric and ionospheric responses to the 21 June 2020 annular solar eclipse. *Earth and Planetary Physics*, *4*(3), 1–7. https://doi.org/10.26464/epp2020032

Dang, T., Lei, J., Wang, W., Zhang, B., Burns, A., Le, H., et al. (2018). Global responses of the coupled thermosphere and ionosphere system to the August 2017 Great American solar eclipse. *Journal of Geophysical Research: Space Physics*, *123*(8), 7040–7050. https://doi.org/10.1029/2018JA025566

Dear, V., Husin, A., Anggarani, S., Harjosuwito, J., & Pradipta, R. (2020). Ionospheric effects during the total solar eclipse over southeast Asia-Pacific on 9 March 2016: Part 1. Vertical movement of plasma layer and reduction in electron plasma density. *Journal of Geophysical Research: Space Physics*, *125*(4), e2019JA026708. https://doi.org/10.1029/2019JA026708

Ding, F., Wan, W., Ning, B., Liu, L., Le, H., Xu, G., et al. (2010). GPS TEC response to the 22 July 2009 total solar eclipse in East Asia. *Journal of Geophysical Research*, *115*(A7), A07308. https://doi.org/10.1029/2009JA015113

Evans, J. V. (1965). On the behavior of f_of_2 during solar eclipses. *Journal of Geophysical Research*, *70*(3), 733–738. https://doi.org/10.1029/JZ070i003p00733

Farges, T., Jodogne, J. C., Bamford, R., Le Roux, Y., Gauthier, F., Vila, P. M., et al. (2001). Disturbances of the western European ionosphere during the total solar eclipse of 11 August 1999 measured by a wide ionosonde and radar network. *Journal of Atmospheric and Solar-Terrestrial Physics*, *63*(9), 915–924. https://doi.org/10.1016/S1364-6826(00)00195-4

Goncharenko, L. P., Erickson, P. J., Zhang, S.-R., Galkin, I., Coster, A. J., & Jonah, O. F. (2018). Ionospheric response to the solar eclipse of 21 August 2017 in Millstone Hill (42N) observations. *Geophysical Research Letters*, *45*(10), 4601–4609. https://doi.org/10.1029/2018GL077334

Hairston, M. R., Mrak, S., Coley, W. R., Burrell, A., Holt, B., Perdue, M., et al. (2018). Topside ionospheric electron temperature observations of the 21 August 2017 eclipse by DMSP spacecraft. *Geophysical Research Letters*, *45*(15), 7242–7247. https://doi.org/10.1029/2018GL077381

Harding, B. J., Drob, D. P., Buriti, R. A., & Makela, J. J. (2018). Nightside detection of a large-scale thermospheric wave generated by a solar eclipse. *Geophysical Research Letters*, *45*(8), 3366–3373. https://doi.org/10.1002/2018GL077015

He, L., Heki, K., & Wu, L. (2018). Three-dimensional and trans-hemispheric changes in ionospheric electron density caused by the Great solar eclipse in North America on 21 August 2017. *Geophysical Research Letters*, *45*(20), 10933–10940. https://doi.org/10.1029/2018GL080365

Huang, F., Li, Q., Shen, X., Xiong, C., Yan, R., Zhang, S.-R., et al. (2020). Ionospheric responses at low latitudes to the annular solar eclipse on 21 June 2020. *Journal of Geophysical Research: Space Physics*, *125*(10), e28483. https://doi.org/10.1029/2020JA028483

Huba, J. D., & Drob, D. (2017). SAMI3 prediction of the impact of the 21 August 2017 total solar eclipse on the ionosphere/plasmasphere system. *Geophysical Research Letters*, *44*(12), 5928–5935. https://doi.org/10.1002/2017GL073549

Jakowski, N., Stankov, S. M., Wilken, V., Borries, C., Altadill, D., Chum, J., et al. (2008). Ionospheric behavior over Europe during the solar eclipse of 3 October 2005. *Journal of Atmospheric and Solar-Terrestrial Physics*, *70*(6), 836–853. https://doi.org/10.1016/j.jastp.2007.02.016

Le, H., Liu, L., Ren, Z., Chen, Y., & Zhang, H. (2020). Effects of the 21 June 2020 solar eclipse on conjugate hemispheres: A modeling study. *Journal of Geophysical Research: Space Physics*, *125*(11), e28344. https://doi.org/10.1029/2020JA028344

Le, H., Liu, L., Yue, X., Wan, W., & Ning, B. (2009). Latitudinal dependence of the ionospheric response to solar eclipses. *Journal of Geophysical Research*, *114*(A7), A07308. https://doi.org/10.1029/2009JA014072

Lei, J., Dang, T., Wang, W., Burns, A., Zhang, B., & Le, H. (2018). Long-lasting response of the global thermosphere and ionosphere to the 21 August 2017 solar eclipse. *Journal of Geophysical Research: Space Physics*, *123*(5), 4309–4316. https://doi.org/10.1029/2018JA025460

Lin, C.-Y., Liu, J.-Y., Lin, C. C.-H., & Chou, M.-Y. (2023). The ionospheric three-dimensional electron density variations induced by the 21 August 2017 total solar eclipse by using global ionospheric specification. *Remote Sensing*, *15*(15), 3887. https://doi.org/10.3390/rs15153887

Liu, J. Y., Sun, Y. Y., Kakinami, Y., Chen, C. H., Lin, C. H., & Tsai, H. F. (2011). Bow and stern waves triggered by the Moon's shadow boat. *Geophysical Research Letters*, *38*(17), L17109. https://doi.org/10.1029/2011GL048805

MacPherson, B., González, S. A., Sulzer, M. P., Bailey, G. J., Djuth, F., & Rodriguez, P. (2000). Measurements of the topside ionosphere over Arecibo during the total solar eclipse of February 26, 1998. *Journal of Geophysical Research*, *105*(A10), 23055–23068. https://doi.org/10.1029/2000JA000145

Momani, M. A., Yatim, B., & Mohd Ali, M. A. (2010). Ionospheric and geomagnetic response to the total solar eclipse on 1 August 2008 over Northern Hemisphere. *Journal of Geophysical Research*, *115*(A8), A08321. https://doi.org/10.1029/2009JA014999

Mrak, S., Semeter, J., Nishimura, Y., Hirsch, M., & Sivadas, N. (2018). Coincidental TID production by tropospheric weather during the August 2017 total solar eclipse. *Geophysical Research Letters*, *45*(20), 10903–10911. https://doi.org/10.1029/2018GL080239

Mrak, S., Zhu, Q., Deng, Y., Dammasch, I. E., Dominique, M., Hairston, M. R., et al. (2022). Modeling solar eclipses at extreme ultra violet wavelengths and the effects of nonuniform eclipse shadow on the ionosphere-thermosphere system. *Journal of Geophysical Research: Space Physics*, *127*(12), e2022JA031058. https://doi.org/10.1029/2022JA031058

Müller-Wodarg, I. C. F., Aylward, A. D., & Lockwood, M. (1998). Effects of a mid-latitude solar eclipse on the thermosphere and ionosphere—A modelling study. *Geophysical Research Letters*, *25*(20), 3787–3790. https://doi.org/10.1029/1998GL900045

Nayak, C., & Yiğit, E. (2018). GPS-TEC observation of gravity waves generated in the ionosphere during 21 August 2017 total solar eclipse. *Journal of Geophysical Research: Space Physics*, *123*(1), 725–738. https://doi.org/10.1002/2017JA024845

Perry, G. W., Watson, C., Howarth, A. D., Themens, D. R., Foss, V., Langley, R. B., & Yau, A. W. (2019). Topside ionospheric disturbances detected using radio occultation measurements during the August 2017 solar eclipse. *Geophysical Research Letters*, *46*(13), 7069–7078. https://doi.org/10.1029/2019GL083195

Reinisch, B. W., Dandenault, P. B., Galkin, I. A., Hamel, R., & Richards, P. G. (2018). Investigation of the electron density variation during the 21 August 2017 solar eclipse. *Geophysical Research Letters*, *45*(3), 1253–1261. https://doi.org/10.1002/2017GL076572

Reinisch, B. W., & Huang, X. (2001). Deducing topside profiles and total electron content from bottomside ionograms. *Advances in Space Research*, *27*(1), 23–30. https://doi.org/10.1016/S0273-1177(00)00136-8

Rideout, W., & Coster, A. (2006). Automated GPS processing for global total electron content data. *GPS Solutions*, *10*(3), 219–228. https://doi.org/10.1007/s10291-006-0029-5

Rishbeth, H. (1968). Solar eclipses and ionospheric theory. *Space Science Reviews*, *8*(4), 543–554. https://doi.org/10.1007/BF00175006

Rishbeth, H., Jenkins, B., & Moffett, R. J. (1995). The F-layer at sunrise. *Annales Geophysicae*, *13*(4), 367–374. https://doi.org/10.1007/s005850050172

Salah, J. E., Oliver, W. L., Foster, J. C., Holt, J. M., Emery, B. A., & Roble, R. G. (1986). Observations of the May 30, 1984, annular solar eclipse at Millstone Hill. *Journal of Geophysical Research*, *91*(A2), 1651–1660. https://doi.org/10.1029/JA091iA02p01651

Silwal, A., Gautam, S. P., Poudel, P., Karki, M., Adhikari, B., Chapagain, N. P., et al. (2021). Global positioning system observations of ionospheric total electron content variations during the 15th January 2010 and 21st June 2020 solar eclipse. *Radio Science*, *56*(5), e2020RS007215. https://doi.org/10.1029/2020rs007215

St.-Maurice, J. P., Ambili, K. M., & Choudhary, R. K. (2011). Local electrodynamics of a solar eclipse at the magnetic equator in the early afternoon hours. *Geophysical Research Letters*, *38*(4), L04102. https://doi.org/10.1029/2010GL046085

Sun, Y.-Y., Liu, J.-Y., Lin, C. C.-H., Lin, C.-Y., Shen, M.-H., Chen, C.-H., & Chou, M.-Y. (2018). Ionospheric bow wave induced by the Moon shadow ship over the continent of United States on 21 August 2017. *Geophysical Research Letters*, *45*(2), 538–544. https://doi.org/10.1002/2017GL075926

Tomás, A. T., Lühr, H., FöRster, M., Rentz, S., & Rother, M. (2007). Observations of the low-latitude solar eclipse on 8 April 2005 by CHAMP. *Journal of Geophysical Research*, *112*(A6), A06303. https://doi.org/10.1029/2006JA012168

Tsai, H. F., & Liu, J. Y. (1999). Ionospheric total electron content response to solar eclipses. *Journal of Geophysical Research*, *104*(A6), 12657–12668. https://doi.org/10.1029/1999JA900001

Vierinen, J., Coster, A. J., Rideout, W. C., Erickson, P. J., & Norberg, J. (2016). Statistical framework for estimating GNSS bias. *Atmospheric Measurement Techniques*, *9*(3), 1303–1312. https://doi.org/10.5194/amt-9-1303-2016

Wang, W., Dang, T., Lei, J., Zhang, S., Zhang, B., & Burns, A. (2019). Physical processes driving the response of the F_2 region ionosphere to the 21 August 2017 solar eclipse at Millstone Hill. *Journal of Geophysical Research: Space Physics*, *124*(4), 2978–2991. https://doi.org/10.1029/2018JA025479

Wu, C., Ridley, A. J., Goncharenko, L., & Chen, G. (2018). GITM-data comparisons of the depletion and enhancement during the 2017 solar eclipse. *Geophysical Research Letters*, *45*(8), 3319–3327. https://doi.org/10.1002/2018GL077409

Yan, M., Dang, T., Lei, J., Wang, W., Zhang, S.-R., & Le, H. (2021). From bow waves to traveling atmospheric disturbances: Thermospheric perturbations along solar eclipse trajectory. *Journal of Geophysical Research: Space Physics*, *126*(4), e28523. https://doi.org/10.1029/2020JA028523

Zhang, S.-R., Erickson, P. J., Goncharenko, L. P., Coster, A. J., Rideout, W., & Vierinen, J. (2017). Ionospheric bow waves and perturbations induced by the 21 August 2017 solar eclipse. *Geophysical Research Letters*, *44*(24), 12067–12073. https://doi.org/10.1002/2017GL076054

Zhang, S.-R., Erickson, P. J., Vierinen, J., Aa, E., Rideout, W., Coster, A. J., & Goncharenko, L. P. (2021). Conjugate ionospheric perturbation during the 2017 solar eclipse. *Journal of Geophysical Research: Space Physics*, *126*(2), e28531. https://doi.org/10.1029/2020JA028531